Magnetic Resonance Imaging 62 (2019) 28–37

Contents lists available at ScienceDirect

Magnetic Resonance Imaging

journal homepage: www.elsevier.com/locate/mri

Original contribution

Common Information Enhanced Reconstruction for Accelerated High-resolution Multi-shot Diffusion Imaging☆

Yuhsuan Wu[a], Xiaodong Ma[b,c], Feng Huang[d], Hua Guo[a,*]

[a] *Center for Biomedical Imaging Research, Department of Biomedical Engineering, School of Medicine, Tsinghua University, Beijing, China*
[b] *Laboratory of Biomedical Imaging and Signal Processing, The University of Hong Kong, Hong Kong, China*
[c] *Department of Electrical and Electronic Engineering, The University of Hong Kong, Hong Kong, China*
[d] *Neusoft Medical System (Shanghai), Shanghai, China*

ARTICLE INFO

Keywords:
Image ratio constrained reconstruction
Common information
SPIRiT
High-resolution DTI
Variable density spiral (VDS)

ABSTRACT

Purpose: Multi-shot technique can effectively achieve high-resolution diffusion weighted images, but the acquisition time of multi-shot technique is prolonged, especially for multiple direction diffusion encoding. Thus, increasing acquisition efficiency is highly desirable for high-resolution diffusion tensor imaging (DTI). In this study, based on the assumption that different diffusion directions share the common information, image ratio constrained reconstruction (IRCR) combined with iterative self-consistent parallel imaging reconstruction (SPIRiT) is proposed to improve data sampling efficiency and image reconstruction fidelity for high-resolution DTI.

Theory and methods: The proposed reconstruction framework is named Common Information Enhanced Reconstruction (CIER). Inter-image correlation among different direction diffusion-weighted images is used through common information, which is an isotropic component and structure, for improving the performance of reconstruction. The framework consists of three steps. (i) Pre-processing: three intermediate multi-shot images, low-resolution composite image, high-resolution composite image and low-resolution diffusion weighted image, are generated based on the SPIRiT method. (ii) IRCR: the initial high–resolution diffusion weighted image is calculated from the images in step (i) based on that the ratio map between high-resolution images is approximated by the ratio map between the corresponding low-resolution images. (iii) Final SPIRiT reconstruction: the final image is generated with the image from IRCR as initialization by considering data consistency only in the SPIRiT calculation. A specific implementation based on multishot variable density spiral (VDS) DTI is used to demonstrate the method.

Results: The proposed CIER method was compared with the traditional reconstruction methods, conjugate gradient SENSE (CG-SENSE), L1-regularized SPIRiT (L1-SPIRiT), and anisotropic-sparsity SPIRiT (AS-SPIRiT) in brain DTI at acceleration factors of 3 to 7. CIER provided better diffusion image quality than other methods shown by both qualitative and quantitative results, especially at higher undersampling acceleration factors.

Conclusion: CIER offers better diffusion image quality at higher undersampling acceleration factors for high-resolution DTI. Both qualitative and quantitative results prove that common information can be used to improve sampling efficiency and maintain the image quality of diffusion-weighted images.

1. Introduction

Diffusion weighted imaging (DWI) can noninvasively probe structural and functional information in the central nervous system, which is important in neuroscience studies and clinical diagnosis [1–3]. Currently, single-shot echo planar imaging (SS-EPI) is widely used for DWI, due to its fast imaging speed and motion insensitivity [4]. However, since SS-EPI has a low bandwidth along the phase encoding (PE) direction, it is sensitive to off-resonance effects caused by field inhomogeneity. Consequently, the images usually have geometric distortions, especially at tissue boundaries with different susceptibilities. Moreover, SS-EPI has a relatively long readout duration compared with

---

☆ Grant sponsor: This work was supported by the National Natural Science Foundation of China (grant number: 61571258) and National Key Research and Development Program of China (grant numbers: 2017YFA0205904 and 2017YFC0108900).

* Corresponding author.
E-mail address: huaguo@tsinghua.edu.cn (H. Guo).

https://doi.org/10.1016/j.mri.2019.05.019
Received 20 February 2019; Received in revised form 3 April 2019; Accepted 14 May 2019
0730-725X/

the transverse relaxation time, which renders SS-EPI prone to blurring artifacts due to the signal decay. Parallel imaging such as sensitivity encoding (SENSE) [5,6] and generalized auto-calibrating partially parallel acquisition (GRAPPA) [9] can be utilized to accelerate k-space traversal and reduce distortions in EPI. However, the improvement is limited because a large acceleration factor can lead to decreased signal-to-noise ratio (SNR) and increased image artifacts [5–9].

To overcome the limitations faced by SS-EPI, multi-shot techniques have been proposed to achieve high-resolution DWI with suppressed image distortions. Using multi-shot methods, the sampling of the k-space is divided into several segments, so that the bandwidth along the PE direction is increased and thus distortion is reduced. One major issue of multi-shot DWI is the different phase variations among different shots, which are induced by involuntary physiological motion. A typical solution to this problem requires a measure of the phase variation by a navigator under the assumption that the navigator shares the same phase variation with the image echo. The navigator is a low-resolution image usually obtained either by using self-navigated methods [5–7], calculated-navigated methods [9–11] or extra-navigated methods [12–20] based on the acquisition and reconstruction strategies. Such strategies have been implemented in interleaved EPI and readout segmented EPI [8–11] as well as non-Cartesian sampling such as periodically rotated overlapping parallel lines with enhanced reconstruction (PROPELLER) [12] and spiral DWI [13–17].

Although multi-shot DWI can effectively improve the resolution and reduce image distortion, it inevitably requires a longer scan time than the single-shot method. This is even more prominent in diffusion tensor imaging (DTI) since it requires at least 6 diffusion encoding directions. As a clinically used fast imaging method, parallel imaging can recover MR images from undersampled data acquired via multi-channel RF coils and has been developed to accelerate multi-shot DWI [7]. Again, as mentioned early, the limitation of parallel imaging is noise amplification, or g-factor, which increases dramatically at larger acceleration factors. In recent years, compressed sensing (CS) is introduced into DWI for fast acquisition [18–24,48,49]. Those methods are based on the hypothesis that medical images have a sparse representation in transform domain. It has shown a great promise for CS to be used for DWI sampling acceleration.

Common information of diffusion weighted images in transform domain was proposed for improving image reconstruction. One method using such a strategy is distributed compressed sensing (DCS) [21–23]. DCS assumes that all the diffusion weighted images from different diffusion encoding directions share the same sparsity support or have joint sparsity property. Simulation and ex-vivo imaging results show that DCS outperforms basic CS (without using the joint sparsity property) in terms of more accurate images and DTI indices. However, DCS is more suitable for DWI with low spatial resolution since CS easily leads to over-smooth in diffusion images. The other method is the low rank model [50], based on the hypothesis that the magnitude of diffusion weighted images is compressible. Nevertheless, this hypothesis is satisfied only when large diffusion encoding directions are used for the imaging. The long computation time can be a big issue as well. Another similar idea based on the common information of diffusion weighted images combined CS and parallel imaging for improved reconstruction fidelity and higher acceleration factors. In addition to intra-image sparsity, inter-image correlation of DWI from multiple diffusion directions was is utilized by enforcing anisotropic sparsity. Based on the general SPIRiT framework, this method was named as anisotropic-sparsity SPIRiT (AS-SPIRiT) [24]. AS-SPIRiT was proven to show superior performance compared with other CS methods, such as DCS.

In this work, we utilize the common information among different direction diffusion images in a different way to improve data sampling efficiency and image reconstruction fidelity for high-resolution DTI. We assume that the difference between the composite image and the reconstructed image is contrast or low frequency signal, which is anisotropic diffusion information in DWI. Thus, the difference between two sets of images can be calculated by their low-resolution images [29–32]. The composite image comes from the common information from neighboring diffusion directions. Based on this assumption, image ratio constrained reconstruction (IRCR) [30,31] is proposed to reconstruct initial diffusion images, which contributes to the further iterative reconstruction by providing the accurate initialization and regularization. Results demonstrate that using the common information can effectively help improve the sampling efficiency and reconstruction, such as L1-regularized SPIRiT (L1-SPIRiT) [33] and AS-SPIRiT, for high-resolution DTI.

2. Theory

2.1. Image ratio constrained reconstruction (IRCR)

We propose to use the pixel-wise ratio map between the calibration image and the reconstructed image as a constraint for reconstruction. The calibration image is the composite image from multiple neighboring diffusion weighted images. The ratio map between high-resolution images is approximated by the ratio map between the corresponding low-resolution images. Therefore, the high resolution image is expressed by the following equation:

$$I_{Rec}^{H}(\vec{x}) \approx I_{C}^{H}(\vec{x}) \bullet \frac{I_{Rec}^{L}(\vec{x})}{I_{C}^{L}(\vec{x})}, \tag{1}$$

where $I_{Rec}^{H}(\vec{x})$ is the high-resolution image to be reconstructed; $I_{Rec}^{L}(\vec{x})$ is the low-resolution DW image calculated from the k-space center of the target diffusion direction; $I_{C}^{H}(\vec{x})$ is the high-resolution composite image, which is calculated from the composite k-space combined by the interleaves from neighboring directions. $I_{C}^{L}(\vec{x})$ is the low-resolution composite image generated by the cropped composite k-space data. The cropped composite k-space data can be obtained directly from the partially acquired k-space center when variable density spiral sampling (VDS) scheme is used. Based on this equation, the reconstructed image of high resolution $I_{Rec}^{H}(\vec{x})$ is estimated by multiplying the composite image of high resolution $I_{C}^{H}(\vec{x})$ with the ratio map between the low-resolution images.

By using Eq. (1) alone to obtain $I_{Rec}^{H}(\vec{x})$, the images still have contamination from other diffusion directions and lose detailed structure. Therefore, the reconstructed result $I_{Rec}^{H}(\vec{x})$ should be Fourier Transformed into k-space and replace the sampled positions with the acquired data in order to keep data consistency. In practice, however, we can never know the exact positions of the original k-space data because they are shifted irregularly by physiological motion, such as cerebrospinal fluid pulsation during the application of diffusion encoding gradients. For multishot DWI, physiological motion can induce shot-to-shot phase variations in image domain due to motion sensitivity of diffusion imaging. The phase changes cause k-space trajectory shift in Fourier domain. As such, instead of replacing the data directly, we use the iterative self-consistent parallel imaging reconstruction, SPIRiT [34], with the estimation from IRCR as the initialization to maintain the data consistency.

2.2. SPIRiT for multi-shot DWI

SPIRiT is used to remove motion induced phase errors in multi-shot acquisitions and reconstruct diffusion weighted images from undersampled data in k-space. In SPIRiT, without considering bulk motion, the k-space data of each channel and each shot can be expressed by the following equation,

$$\boldsymbol{d}_{\boldsymbol{n},\boldsymbol{s}} = \boldsymbol{F}_{\boldsymbol{s}} \boldsymbol{G}_{\boldsymbol{s}} \boldsymbol{P}_{\boldsymbol{s}} \boldsymbol{m}_{\boldsymbol{n},} \mathrm{n} = 1,\ \ldots, N_c;\ \mathrm{s} = 1,\ \ldots, N_s, \tag{2}$$

where $\boldsymbol{P}$ is the phase error which can be estimated using navigator data; $\boldsymbol{G}$ is the gridding operator and $\boldsymbol{F}$ is the Fourier transformation operator. In this paper, $\boldsymbol{F}$ is Non-uniform Fourier transform (nuFT) for non-

Cartesian trajectory, and the algorithm we used here is non-uniform fast Fourier transform (NUFFT) [35]; $\boldsymbol{d}$ is the acquired k-space data; $\boldsymbol{m}$ is the image to be solved; N_c and N_s represent channel number and shot number, respectively. In multishot DWI using VDS, phase error $\boldsymbol{P}$ is estimated in the same way as introduced in [7]. Specifically, the k-space center of each shot, which is close to fully-sampled, is extracted by applying a Gaussian window, and the phase of the reconstructed low-resolution image can be used for motion-induced phase correction. $\boldsymbol{P}$ operates by first multiplying the image $\boldsymbol{m}$ with the estimated shot-by-shot varying motion-induced phase, and then applying NUFFT.

The formula to determine the n-th image $\boldsymbol{m}_n$ is

$$\widehat{\boldsymbol{m}}_n = \underset{m_n}{argmin}\left[\sum_{s=1}^{N_S} \|\boldsymbol{F}_s\boldsymbol{P}_s\boldsymbol{m}_n - \boldsymbol{d}\|_{L2} + \lambda_1 \|(\boldsymbol{C}-\boldsymbol{I})\boldsymbol{m}_n\|_{L1} + \lambda_2\boldsymbol{\psi}(\boldsymbol{m}_n)\right], \tag{3}$$

where $\boldsymbol{C}$ is the self-calibrating operator in image domain, which is a multiplication operation with inverse.

Fourier transform of the k-space convolution kernels; $\boldsymbol{I}$ is the identity matrix and $\boldsymbol{\psi}$ is the wavelet transformation operator. $L1$ and $L2$ represent corresponding norm. λ_1 and λ_2 are the weighting factors of self-calibration and regularization terms, respectively. In the Eq. (3), the first term is the data consistency, the second term is calibration consistency, and the third term is wavelet regularization.

To calculate the operator $\boldsymbol{C}$, two-step SPIRiT is required. In the first step, λ_1 is set to be zero such that only the term of data consistency and the wavelet regularization are minimized. In the second step, $\boldsymbol{C}$ is extracted from the image of the first step of SPIRiT, which is free of phase error. We minimized the entire equation together. By doing this, data consistency and calibration consistency are enforced in separate terms in the reconstruction formulation; operator $\boldsymbol{C}$ is free from effects of different sampling trajectories and interleaf-varying phase errors, thus making the calibration process highly flexible [24].

As for the algorithm, the conjugate gradient method is used to iteratively compute the desired image [36–38]. In addition, λ_1 in Eq. (3) was searched from 0 to 1 in the second step. λ_2 was searched from 1e-6 to 0.1, based on the experience and normalized root-mean-square deviation (nRMSE) which will be mentioned in Methods section.

2.3. Reconstruction framework

The full reconstruction consists of three steps and generates four intermediate images, $I_{Rec}{}^{L}(i)$, $I_C{}^{L}(i)$, $I_C{}^{H}(i)$, $I_{Rec}{}^{H}(i)$ and one final reconstructed image, $I_{CIER}(i)$, where i represents the ith diffusion direction. Fig. 1 shows the flowchart of the reconstruction.

1. Pre-processing: generation of low-resolution DW image ($I_{Rec}{}^{L}$), low-resolution composite image ($I_C{}^{L}$), and high-resolution composite image, ($I_C{}^{H}$). The pre-processing procedure is demonstrated in the following steps.

    a. In the ith direction (i = 1, 2, … N, N is the number of diffusion directions), center k-space data are cropped from acquired k-space followed by two-step SPIRiT to reconstruct a low-resolution DW image, $I_{Rec}{}^{L}(i)$. In the first step of SPIRiT, λ_1 in Eq. (3) is set as zero. That is, only the term of data consistency and the wavelet regularization are minimized. Next step, $\lambda_1$and λ_2 use non-zero parameters for minimizing the whole Eq. (3).
    b. The k-space data from neighboring directions are combined to form the composite k-space data followed by two-step SPIRiT to generate a high-resolution composite image, $I_C{}^{H}(i)$. The parameters of SPIRiT are the same as the step (a).
    c. The composite k-space data are cropped directly from the partially acquired k-space center to generate a low-resolution composite image, $I_C{}^{L}(i)$. The reconstruction method consists of two-step SPIRiT as well.

    Note that λ_1 is 1 and λ_2 is 0.01 in this pre-processing step.

2. IRCR: generation high-resolution initial image ($I_{Rec}{}^{H}$). The model applied here is Eq. (1). The IRCR ratio map, $\frac{I_{Rec}^{L}(i)}{I_C^{L}(i)}$, is calculated by the low-resolution images from the composite images and the DW images from the previous step. After that, we use the IRCR ratio map and high-resolution composite image to calculate high-resolution image, $I_{Rec}{}^{H}(i)$.
3. Final reconstruction: generation of final image (I_{CIER}). This step is to guarantee the consistency between the reconstructed images and the acquired k-space data since there still exists contamination from other diffusion directions after the image ratio calculation. In this step, iterative reconstruction is implemented with the result of IRCR, $I_{Rec}{}^{H}$, as the initial guess. The model applied here is same as Eq. (3):

$$\widehat{\boldsymbol{I}_{\boldsymbol{Rec}\,n}^{\boldsymbol{H}}}(i) = arg \min_{\boldsymbol{I}_{\boldsymbol{Rec}}^{\boldsymbol{H}}(\boldsymbol{n})}\left[\sum_{s=1}^{N_S} \|\boldsymbol{F}_s\boldsymbol{P}_s\boldsymbol{I}_{\boldsymbol{REC}_n}^{\boldsymbol{H}}(\boldsymbol{i}) - \boldsymbol{d}\|_{L2} + \lambda_1 \|(\boldsymbol{C}-\boldsymbol{I})\boldsymbol{I}_{\boldsymbol{REC}_n}^{\boldsymbol{H}}(\boldsymbol{i})\|_{L1} + \lambda_2\boldsymbol{\psi}(\boldsymbol{I}_{\boldsymbol{REC}_n}^{\boldsymbol{H}}(\boldsymbol{i}))\right]. \tag{4}$$

where $\widehat{\boldsymbol{I}_{\boldsymbol{Rec}\,n}^{\boldsymbol{H}}}(i)$ is the final image, I_{CIER}. In practice, a non-zero with very small λ_1 is used to make the reconstruction more stable. In particular, λ_1 is set to be 0.1 and λ_2 is set to be 0.005 in this step. The corresponding operator $\boldsymbol{C}$ is extracted from $I_{Rec}{}^{H}$.

3. Methods

3.1. Data acquisition

In this paper, VDS with complementary trajectories [39] is used to acquire diffusion imaging data. For example, in VDS DTI with 6*M interleaves as full sampling, if acceleration factor is 6, for the first direction, data of M interleaves is collected; for the next direction, k-space is also traversed with M interleaves but the trajectory is turned by an angle of 2π/R (R: undersampling factor, which is 6 here) over the previous one. By doing this, k-space along one selected direction can be combined with its nearby directions to generate a full-sampled or oversampled k-space at the k-space edge. Therefore, the complementary information can be used effectively. Please refer to Data acquisition box in Fig. 1 for details about data sampling for composite k-space formation. Different colors represent undersampled interleaves from different diffusion directions. Different direction has different rotated spiral interleaves.

To apply CIER to human brain DWI, 4 experiments were conducted to test different aspects of the proposed method on a Philips 3T clinical scanner (Achieva, Philips, Best, The Netherlands) with an 8-channel head coil. All experiments used a multishot VDS sequence, which is the same as in [24,39]. The common parameters for these 4 scans were: $\alpha = 4$, slice thickness = 5 mm, and FOV = 220 × 220 mm^2. α controls the sampling density along the radial direction for the spiral trajectory. Other parameters were listed in the Table 1. In particular, for experiment 4, reference images were obtained by averaging over the repeated acquisitions.

All human studies were performed under Institutional Review Board approval from our institution. Informed consent was obtained from each volunteer before the experiments.

3.2. Data processing

To compare with the proposed framework, the traditional methods, conjugate gradient SENSE (CG-SENSE) [7] and SPIRiT-based methods, L1-SPIRiT [33] and AS-SPIRiT [24], were implemented. In addition, both L1-SPIRiT and AS-SPIRiT can be used in the pre-processing step and the third step of CIER. When CIER is combined with L1-SPIRiT, we call it CIER-SPIRiT. When CIER is combined with AS-SPIRiT, we call it CIER-AS-SPIRiT. In summary, the undersampled sets of data were

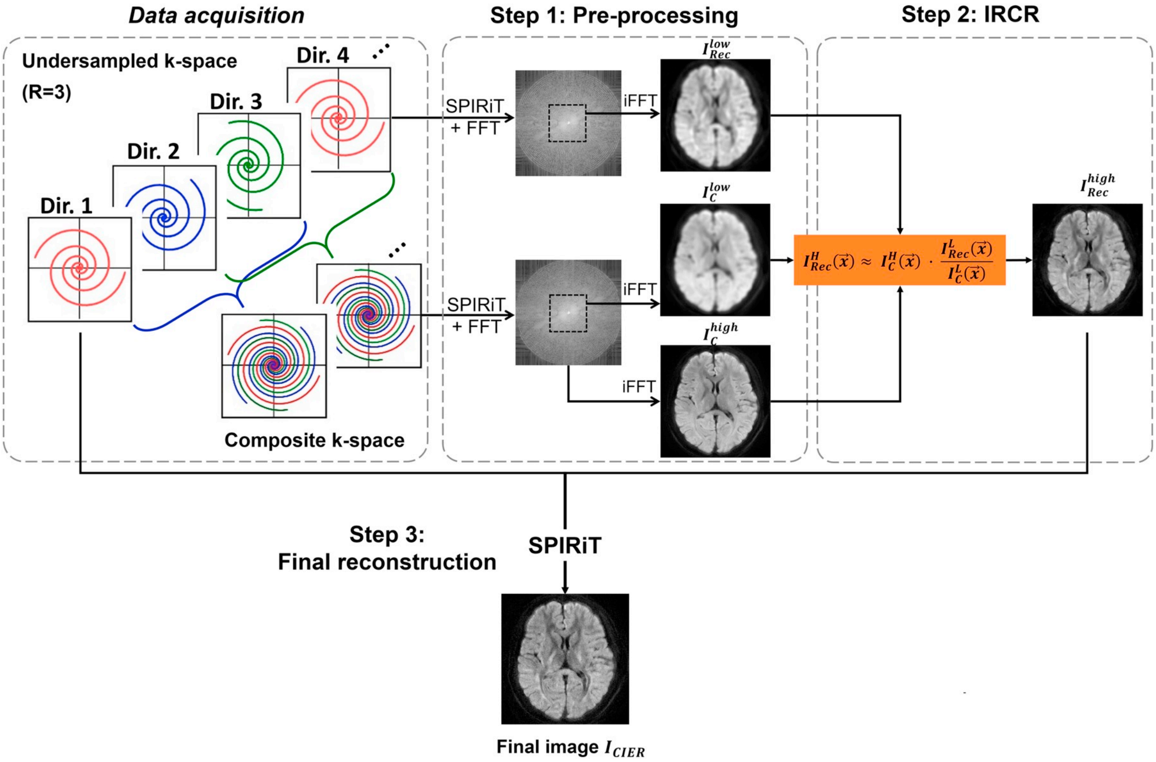

Fig. 1. Flowchart of signal sampling and image reconstruction for VDS-DWI. First, the partially acquired k-space data of each direction are processed using simultaneous phase correction (PC) and SPIRiT reconstruction. Second, Image ratio constrained reconstruction (IRCR) is used to generate the initial reconstruction of each direction by compositing k-space with nearby diffusion directions. Last, SPIRiT is used again to generate the final reconstruction iteratively, using the image with high SNR by IRCR as initialization. In Data acquisition box, different colors of the sampling trajectory represent the interleaves acquired in each diffusion direction. With combining the k-space of different colors, the composite k-space is fully-sampled. In the figure, R is 3 so there are three different colors. (For interpretation of the references to color in this figure legend, the reader is referred to the web version of this article.)

reconstructed by (i) CIER-SPIRiT, (ii) CIER-AS-SPIRiT, (iii) CG-SENSE, (iv) L1-SPIRiT, and (v) AS-SPIRiT, as listed in Table 2.

The undersampled data were artificially undersampled from fully-sampled data using reduction factors ranging from R = 3 to 7. The acceleration factor we used here was undersampled interleaves. For example, to obtain a reduction factor of R, one in every R spiral interleaves was sampled. Therefore, after data undersampling, the data were either over-sampled or fully-sampled in k-space center and undersampled at the edge. In the diffusion direction dimension, complementary sampling trajectory was adopted as introduced before.

All reconstruction methods were performed on the same set of undersampled data as mentioned above. Reference images were reconstructed by L1-SPIRiT from fully-sampled data with phase correction. Blurring artifacts caused by off-resonance need to be suppressed since spiral trajectories are used. Instead of acquiring additional field maps to demodulate the original k-space data, automatic off-resonance correction without field maps [40,41] was implemented here to post-process both the reconstructed image and reference images.

After the reconstruction of DW images, color-coded fractional anisotropy (FA) maps were calculated by FSL [42] for qualitative comparison. Root-mean-square deviation (RMSE), normalized root-mean-square deviation (nRMSE) and SNR were used for quantitative comparison [24,43,44]. The formula of RMSE is defined as,

Table 2
The rows, from top to bottom, are different methods implemented in this paper. The columns, from left to right, are the name of the methods, its algorithm, its computational time in experiment 1 at R = 5, and its computational time in experiment 3 at R = 5.

Method	Algorithm	Experiment 1 Time (s)	Experiment 3 Time (s)
CG-SENSE	CG-SENSE	30.62	114.86
L1-SPIRiT	SPIRiT + wavelet sparsity	91.23	574.98
AS-SPIRiT	SPIRiT + anisotropic sparsity + wavelet sparsity	88.06	575.60
CIER-SPIRiT	CIER + L1-SPIRiT	94.10	675.91
CIER-AS-SPIRiT	CIER + AS-SPIRiT	108.74	745.02

Table 1
The parameters of four experiments.

Experiment	b-value (s/mm^2)	TR/TE (ms)	Number of directions	Number of interleaves	NSA	Matrix size	Image resolution (mm × mm)	Readout length (ms)	Sampling points
1	800	2100/64	6	24	1	256 × 256	0.85 × 0.85	18.0	4334
2	800	2100/64	32	18	1	256 × 256	0.85 × 0.85	25.6	5634
3	800	2200/64	48	18	1	256 × 256	0.85 × 0.85	25.6	5062
4	1600	2100/64	6	24	2	200 × 200	1.00 × 1.00	10.0	2949

Note that NSA is number of signal averages.

$$\mathrm{RMSE} = \sqrt{\frac{\sum_{r\in ROI}(m_{ref}(r) - \widehat{m}(r))^2}{N_{r\in ROI}}}, \tag{5}$$

where m_{ref} is the reference FA map reconstructed from full-sampled data; $\widehat{m}$ is the FA map reconstructed from undersampled data; r represents spatial location. The whole brain was selected as region of interest (ROI), and $N_{r\in ROI}$ is the number of pixels in the ROI.

The formula of nRMSE is defined as,

$$\mathrm{nRMSE} = \sqrt{\frac{\sum_{r\in ROI}(m_{ref}(r) - \widehat{m}(r))^2}{\sum_{r\in ROI}(m_{ref}(r))^2}}, \tag{6}$$

The ROI was selected to be the diffusion images of all diffusion directions.

The formula of SNR is defined as,

$$\mathrm{SNR}(k_1, k_2) = \frac{mean_{r\in ROI}(S(r, k_1) + S(r, k_2))}{\sqrt{2}\, stddev_{r\in ROI}(S(r, k_1) - S(r, k_2))}, \tag{7}$$

where k_1, k_2 are two identical acquisitions; $S(r, k_1)$ refers to signal intensity of the voxel at location r in acquisition k_1. In experiment 3, two repeat acquisitions were acquired to calculate the SNR value. The ROI was selected to be the diffusion images of all diffusion directions.All reconstruction methods were conducted in Mathworks on a Linux workstation with a 2.0 GHz CPU and 128 GB of RAM. The computational time of all the methods in experiment 1 and 3 were calculated.

4. Results

4.1. Experiment 1

Fig. 2 shows the results reconstructed by the proposed method and the comparisons with CG-SENSE, L1-SPIRiT, and AS-SPIRiT in experiment 1 at R = 5. In the second column of Fig. 2, CG-SENSE suffers more serious artifacts and noise amplification in the most area of the brain compared with other algorithms. In addition, the corresponding noise level and nRMSE are relatively higher in CG-SENSE. L1-SPIRiT also results in a larger error level compared with AS-SPIRiT and CIER-SPIRiT, indicating that the common information in DW images used by the latter counterparts helps improve reconstruction performance. Compared with AS-SPIRiT, CIER-SPIRiT provides a lower error level in DWIs as demonstrated by the difference maps in the second row of Fig. 2. Additionally, the error distribution of CIER-SPIRiT is more uniform than other reconstruction methods.

The corresponding color-coded FA maps, FA maps, and the difference maps of experiment 1 at R = 5 are shown in Fig. 3 for further demonstration. RMSEs of the FA maps from all methods are displayed at the bottom of Fig. 3. In the color-coded FA maps, the directionality in AS-SPIRiT and CIER-SPIRiT are closer to the reference than in CG-SENSE and L1-SPIRiT. Severe false directionality appears in the results of CG-SENSE and such errors are reduced in the results of AS-SPIRiT and CIER-SPIRiT. The performance of AS-SPIRiT and CIER is of small difference in the FA maps in this experiment. The results indicate that the common information among different diffusion directions can improve the reconstruction fidelity.

4.2. Experiment 2

In theory, the composite k-space should be made from nearby diffusion directions in order to minimize contamination. If the directions are closer, the common information should be shared more. Therefore, the reconstructed image quality is supposed to be better. Based on this assumption, if the distance between the directions is short, more number of diffusion directions can be selected to improve signal undersampling rates.

In experiment 2, again we set the undersampling factor R = 5. Then the composite k-space was formed from the closest 4 diffusion directions among the 32 directions. In addition, instead of using the closest directions, we first selected 6-direction data uniformly from the 32-direction data and then used all direction data to form the composite k-space. Furthermore, we selected 10 directions uniformly from the 32-direction data. Then we used the closest 4-direction data to form another set of composite k-space. We expect to observe the effect of number of diffusion directions on our proposed method, or to study the effect of diffusion direction distance on the reconstruction. Table 3 shows the nRMSE values from different methods for the three datasets. L1-SPIRiT and AS-SPIRiT give similar results in the three datasets. However, nRMSEs from CIER-SPIRiT and CIER-AS-SPIRiT become smaller with the increase in the number of directions. The reason should be the higher signal similarity for closer direction data.

4.3. Experiment 3

Fig. 4 shows the results in experiment 3 with R changing from 3 to 7. Here AS-SPIRiT was chosen as pre-processing, thus the reconstruction became CIER-AS-SPIRiT. The maximum R factor for AS-SPIRiT in the previous paper [24] was 6. Here, we compared CIER-AS-SPIRiT with AS-SPIRiT. Both CIER-AS-SPIRiT and AS-SPIRiT perform well with low acceleration factors, such as R = 3 or R = 5. However, AS-SPIRiT

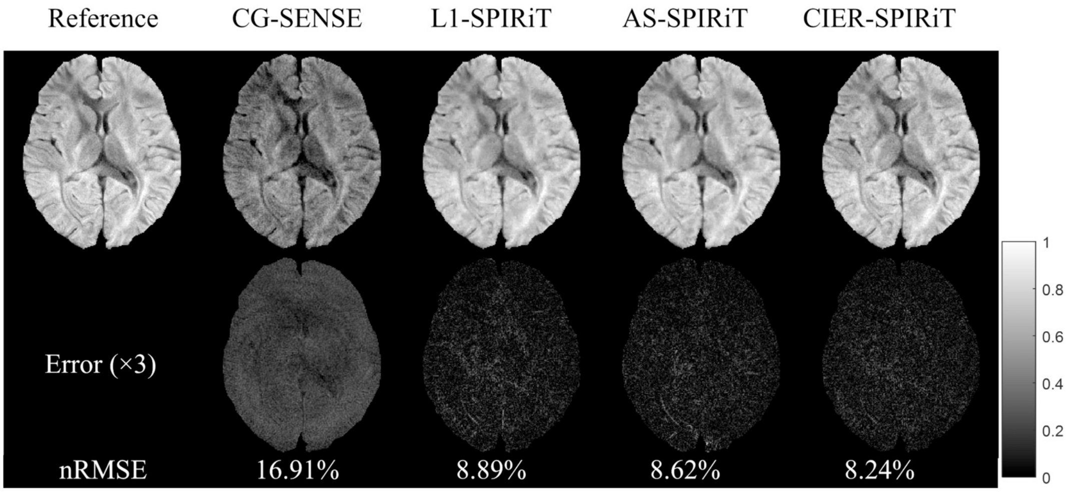

Fig. 2. Representative diffusion weighted images in experiment 1 when R = 5. The upper row shows one of the representative DW images, and the lower row shows corresponding difference images (scaled by a factor of 3). The columns, from left to right, are reference image and results of CG-SENSE, L1-SPIRiT, AS-SPIRiT, and CIER-SPIRiT at R = 5, respectively. The corresponding nRMSEs from those methods are shown in the bottom of figures.

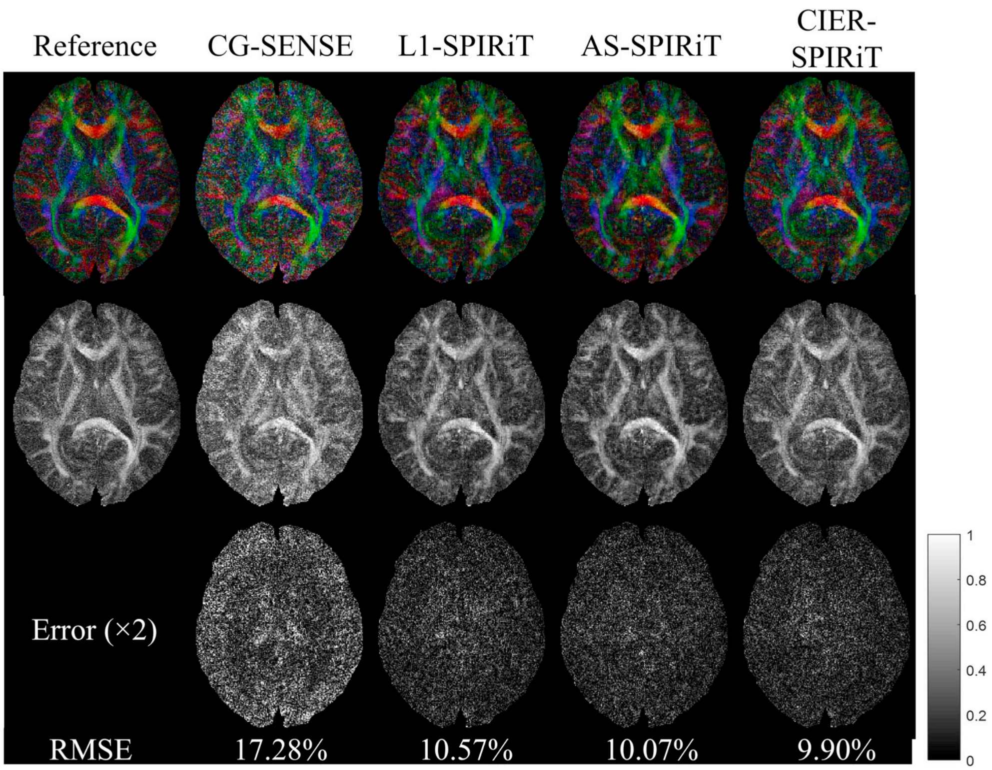

Fig. 3. Comparison of FA maps in experiment 1. The rows from top to bottom are color-coded FA (red: right-left, green: anterior–posterior; blue: dorsal–ventral), FA and difference images of FA at R = 5. The columns, from left to right, are the reference and results of CG-SENSE, L1-SPIRiT, AS-SPIRiT, and CIER-SPIRiT at R = 5. The corresponding RMSEs of those methods are shown in the bottom of figures. (For interpretation of the references to color in this figure legend, the reader is referred to the web version of this article.)

Table 3
nRMSE of diffusion weighted images at R = 5 in Experiment 2 with 6 directions, 10 directions, 32 directions.

	6 directions	10 directions	32 directions
L1-SPIRiT	0.105	0.105	0.105
CIER-SPIRiT	0.084	0.082	0.081
AS-SPIRiT	0.105	0.105	0.105
CIER-AS-SPIRiT	0.080	0.080	0.079

suffers serious artifacts at high acceleration factors while CIER-AS-SPIRiT maintains better reconstruction performance. The difference maps further indicate that the error level from CIER-AS-SPIRiT is lower than that from AS-SPIRiT at R = 6 or R = 7 as shown in the right 2 columns in Fig. 4. The difference can be observed more clearly from the enlarged parts of images in the bottom-right corner of each image. The performance of the proposed method is further compared with AS-SPIRiT quantitatively by nRMSE with different R values in the bottom of each image. It shows that CIER-AS-SPIRiT has better reconstruction quality in the explored range of reduction factors. Using the 2 lower reduction factors, the difference between nRMSEs from the two methods is not as big as that using the 2 higher reduction factors. In other words, the difference increases as the reduction factor increases. It again proves that CIER-AS-SPIRiT is able to maintain better reconstruction quality as reduction factor increases.

The corresponding FA maps from experiment 3 for qualitative comparison are shown in Fig. 5. Again, as in Fig. 5, the results show that both AS-SPIRiT and CIER-AS-SPIRiT have low error levels at R = 3 or R = 5. When R is larger than 5, the FA maps of AS-SPIRiT can't preserve the fine structure. In comparison, CIER-AS-SPIRiT still has a lower error level, especially at the area pointed by the arrows in Fig. 5. Additionally, the false directionality is apparent at the center of the brain in AS-SPIRiT. Therefore, CIER-AS-SPIRiT provides lower error level at the higher acceleration factors.

4.4. *Experiment 4*

The proposed reconstruction was also explored at a high b value of 1600 s/mm^2 in experiment 4. High b values with high resolution can result in a lower SNR so the acceleration factor R is limited. Again, AS-SPIRiT was chosen as pre-processing, and the reconstruction became CIER-AS-SPIRiT. Fig. 6 demonstrates the performance of AS-SPIRiT and CIER-AS-SPIRiT at this high b value with the reconstructed diffusion weighted images and the corresponding FA maps. The corresponding difference map is shown correspondingly. Also, we calculated nRMSE of the diffusion weighted images and RMSE of the FA maps. The quantitative numbers show that CIER-AS-SPIRiT has lower nRMSE and RMSE than AS-SPIRiT. Thus, our proposed method still shows the improved performance than the compared one when image SNR is low.

Furthermore, more quantitative information about the performance comparison of three methods is shown in Fig. 7. nRMSE and SNR were calculated from experiment 4 at R = 3 to 6. SNR was calculated using Eq. (7). Compared with L1-SPIRiT, AS-SPIRiT and CIER-AS-SPIRiT preserve higher SNRs for $R \leq 5$. However, SNR from AS-SPIRiT declines rapidly with the increase of R to 6. It drops almost 25.4% at R = 6 while CIER-AS-SPIRiT still has higher SNR and lower nRMSE. The figure again reveals that CIER is a useful enhancing technique, which yields better reconstruction fidelity.

4.5. *Computational cost*

The computational costs of all methods in experiment 1 and experiment 3 are listed in Table 2. Since our method is based on the outcome of SPIRiT, its reconstruction time is slightly longer than that of AS-SPIRiT and SPIRiT. CIER-AS-SPIRiT took 119%~129% of the time that AS-SPIRiT used.

5. Discussion

Although high-resolution DTI is a useful and promising technique in

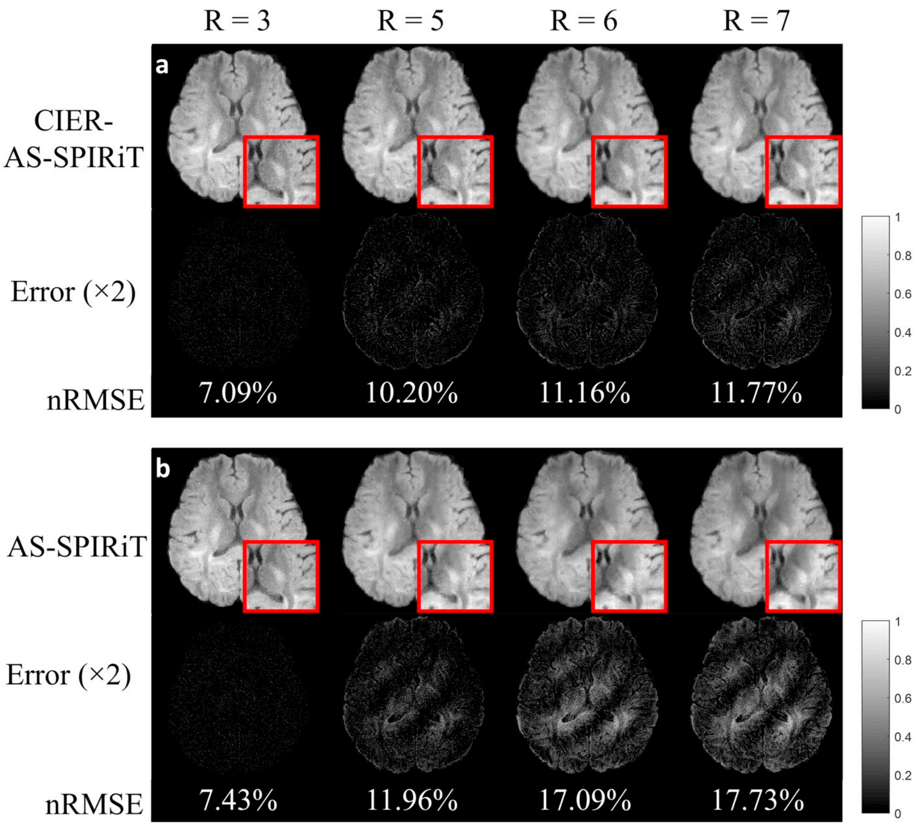

Fig. 4. Representative DW images in experiment 3 with different R for CIER-AS-SPIRiT and AS-SPIRiT. An enlarged portion of the image is displayed at the bottom-right corner of each image. (a) It shows the results of CIER-AS-SPIRiT and the difference maps (scaled by a factor of 2). The columns, from left to right, are results with accelerating factor from R = 3 to 7. The corresponding nRMSEs of CIER-AS-SPIRiT in different R are shown in the bottom of figures. (b) It shows the results of AS-SPIRiT and the difference maps (scaled by a factor of 2).

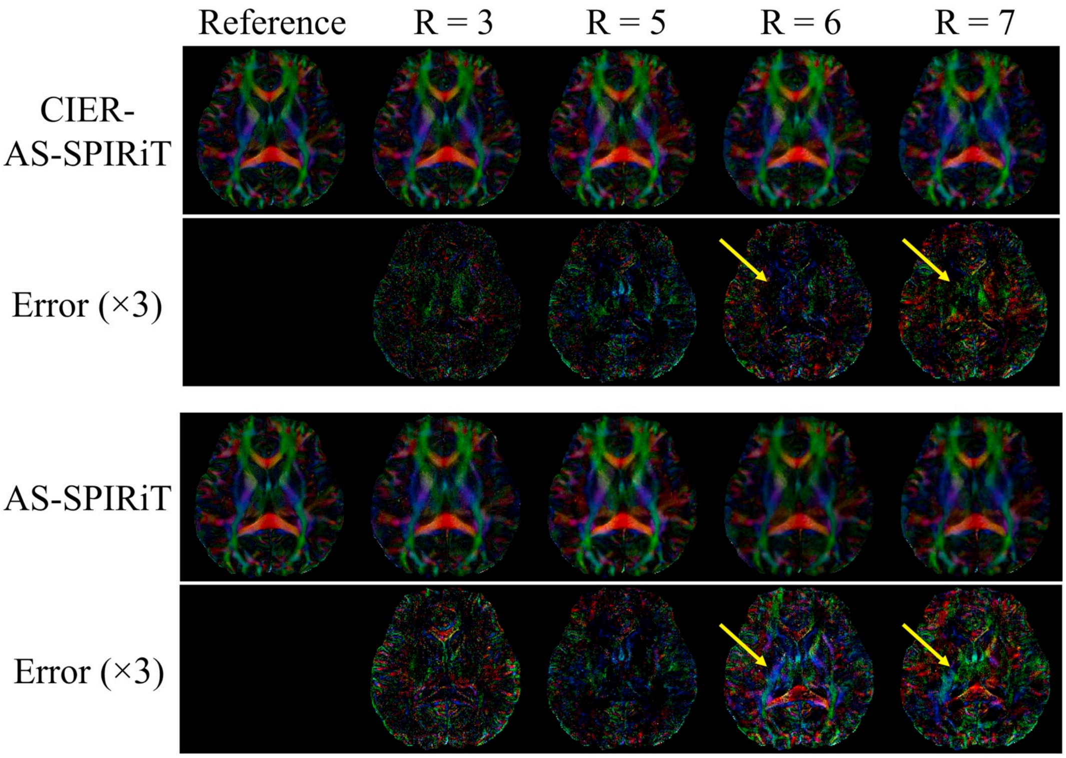

Fig. 5. Representative FA maps in experiment 3 with different R for CIER-AS-SPIRiT and AS-SPIRiT. (a) It shows the color-coded FA map of CIER-AS-SPIRiT and the difference FA maps (scaled by a factor of 5). The columns, from left to right, are results with accelerating factor from R = 3 to 7. (b) It shows the color-coded FA maps of AS-SPIRiT and the error FA maps (scaled by a factor of 5). The yellow arrows point out where large error appears in the FA maps of AS-SPIRiT and where the error is reduced in CIER-AS-SPIRiT. (For interpretation of the references to color in this figure legend, the reader is referred to the web version of this article.)

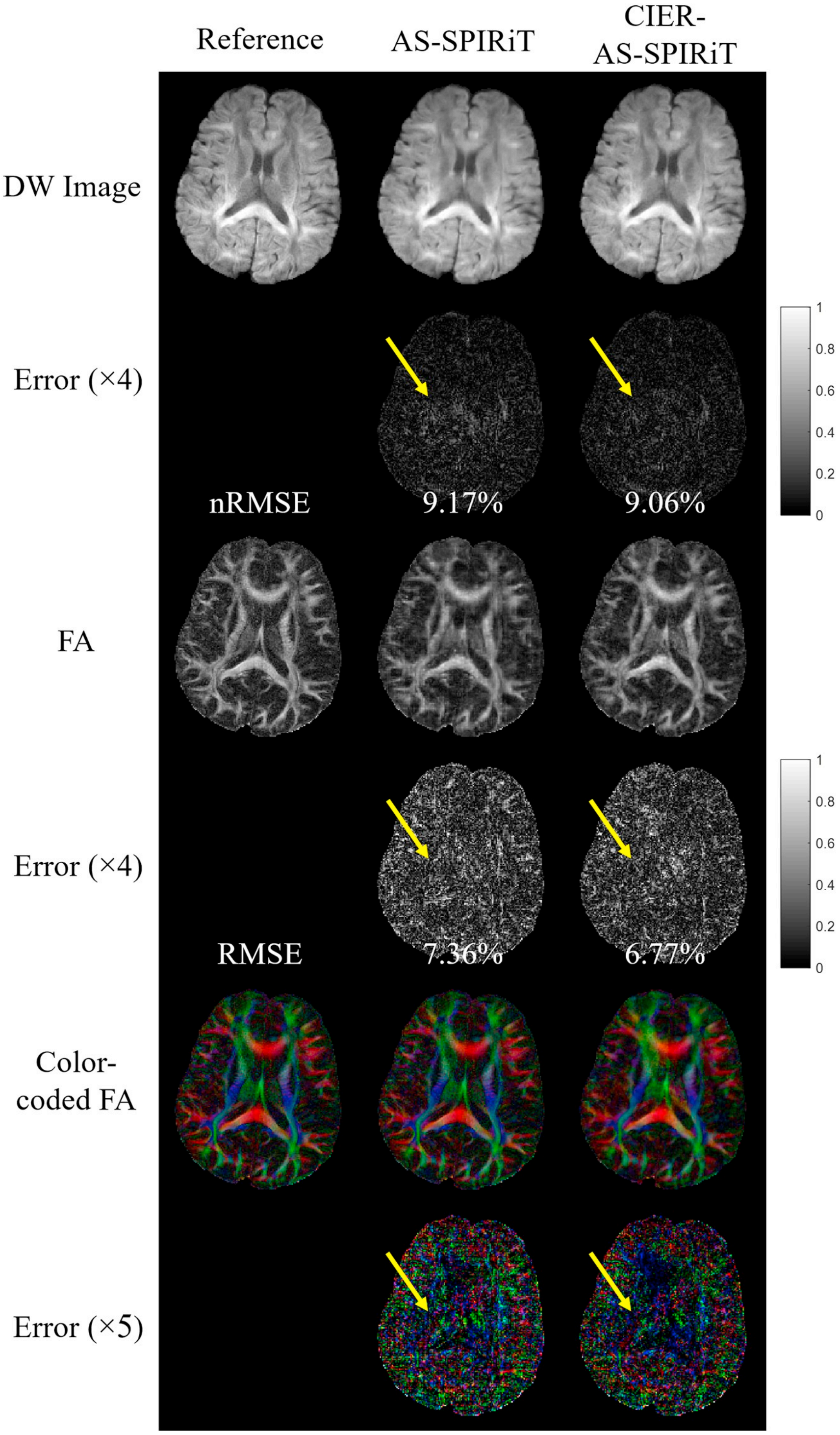

Fig. 6. Comparison of results in experiment 4 with b = 1600 s/mm^2. The columns, from left to right, are the reference and the results from AS-SPIRiT and CIER-AS-SPIRiT at R = 4. The corresponding nRMSEs and RMSE of those methods are shown in the bottom of each difference map. The yellow arrow points out where large error appears in the FA maps of AS-SPIRiT and where the error is reduced in CIER-AS-SPIRiT. (For interpretation of the references to color in this figure legend, the reader is referred to the web version of this article.)

neuroimaging studies and clinical diagnosis, SNR and acquisition time have always been obstacles in its practical applications. Thus, improving spatial resolution while maintaining SNR and time efficiency in DTI is always desired. Traditional PI methods, such as CG-SENSE and GRAPPA, have long been attempted in accelerating high-resolution DTI [7–9], but reached their bottleneck in acceleration capability due to noise amplification and residual aliasing at high acceleration factors. In the meantime, previous work had demonstrated the great potential of common information for diffusion image reconstruction in order to increase signal sampling efficiency [24]. In this study, the proposed strategy, CIER, takes advantage of common information in DTI reconstruction by using neighboring images from a different perspective. Since CIER is a 2D imaging technique, it can further boost the acceleration through combining with other fast-imaging techniques, such as simultaneous multislice (SMS) [45] imaging.

In this study, the proposed reconstruction was compared with CG-

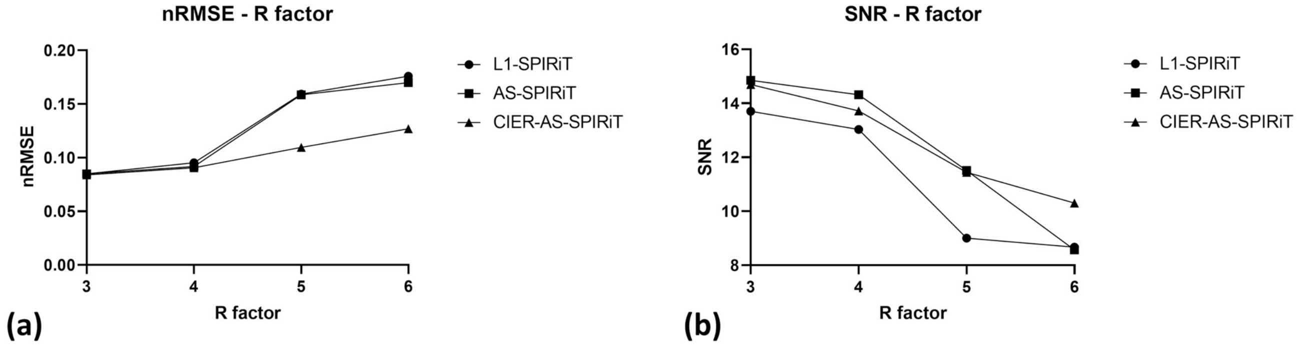

Fig. 7. Quantitative comparison of the results from R = 3 to 6 in experiment 4. (a) nRMSE of diffusion images from L1-SPIRiT (circles), AS-SPIRiT (squares), and CIER-AS-SPIRiT (triangles). (b) SNR of diffusion images from L1-SPIRiT (circles), AS-SPIRiT (squares), and CIER-AS-SPIRiT (triangles).

SENSE which had only been tried with the acceleration factor of 3 for high resolution VDS-DTI [7], and SPIRiT based methods which had only been tried with the acceleration factor of 5 [24]. The previous studies have shown that SPIRiT based methods are more superior to CG-SENSE. In addition, AS-SPIRiT has been proven to have better performance than L1-SPIRiT [24]. In the experiments here, with low acceleration factors, the difference between AS-SPIRiT and CIER is not obvious in both experiments 1 and 3. We believe that AS-SPIRiT has reliable reconstruction capability at low acceleration factors. However, when R = 6 or R = 7, CIER provides improved reconstruction quality than the compared methods in both two experiments. It proves that CIER is also suitable for high undersampling acceleration factors. IRCR can be combined with any kinds of SPIRiT methods. By combing with superior SPIRiT-based methods, such as AS-SPIRiT, it can achieve higher undersampling acceleration factors and better image accuracy. For example, when R = 6 in experiment 3, nRMSE can be reduced from 0.1709 from AS-SPIRiT to 0.1116 from CIER-AS-SPIRiT.

When using CIER to reconstruct multi-direction diffusion images, data selection to form the composite k-space needs attention. Ideally, data should be selected from as close directions as possible to form the fully-sampled k-space. For high angular diffusion imaging, such as 32 or 48 directions in this study, the selected data come from closer neighbors, thus the contamination is less than for fewer direction diffusion imaging. We refer the interested readers to our previous work more detailed descriptions [46].

One concern of our method is the blurring issue. When selecting the parameters, λ_1 and λ_2, nRMSE can be the justification to choose the proper values. However, the reconstructed image may be blurred if nRMSE is the only standard. Therefore, a better strategy to select the parameters is based on both nRMSE and visual observation. Our experience is that choosing smaller λ_1 and λ_2 at the last step of the framework can mitigate the blurring effect in reconstructed images. Furthermore, L1-SPIRiT and AS-SPITiT also have blurring effect, especially at high acceleration factors. For example, in Fig. 4, blurring effect in images from AS-SPIRiT is stronger with the increase of the R factors. The blurring effect can be observed clearly from the enlarged parts of images in the bottom-right corner of each image.

One drawback of using common information for image reconstruction is the mis-registration introduced by motion. Although physiological motion induced phase error can be resolved in DTI reconstruction via SPIRiT, macroscopic motion can bring severe problems to the reconstruction. Because of the motion, the geometry of images will be different, and we cannot assume that they share similar structures anymore. Thus motion correction and image registration are needed [47]. Using common information to acquire less data may reduce the motion effect because less imaging time is required.

6. Conclusion

In this study, a reconstruction method for accelerating multishot high-resolution DTI, which combined IRCR and SPIRiT, was developed. It takes advantage of the characteristic of the diffusion imaging by utilizing the similar information from different direction images efficiently. This proposed method was assessed and compared with the traditional techniques in in-vivo DTI experiments qualitatively and quantitatively. The proposed CIER method offers an effective way for accelerating high-resolution DTI.

Acknowledgments

This work was supported by the National Natural Science Foundation of China (grant number: 61571258) and National Key Research and Development Program of China (grant numbers: 2017YFA0205904 and 2017YFC0108900).

References

[1] Turner R, Le Bihan D, Chesnicks AJMrim Scott. Echo-planar imaging of diffusion and perfusion. 1991;19(2):247–53.

[2] Haselgrove JC, Moore JRJMRiM. Correction for distortion of echo-planar images used to calculate the apparent diffusion coefficient. 1996;36(6):960–4.

[3] Le Bihan D, et al. Diffusion tensor imaging: concepts and applications. 2001;13(4):534–46.

[4] van Pul C, et al. A comparison study of multishot vs. single-shot DWI-EPI in the neonatal brain: reduced effects of ghosting compared to adults. vol. 22(9). 2004. p. 1169–80.

[5] Bammer R, et al. Diffusion tensor imaging using single-shot SENSE-EPI. 2002;48(1):128–36.

[6] Bammer R, et al. Improved diffusion-weighted single-shot echo-planar imaging (EPI) in stroke using sensitivity encoding (SENSE). vol. 46(3). 2001. p. 548–54.

[7] Liu C, Moseley ME, Bammer R. Simultaneous phase correction and SENSE reconstruction for navigated multi-shot DWI with non-Cartesian k-space sampling. 2005;54(6):1412–22.

[8] Holdsworth SJ, et al. Readout-segmented EPI for rapid high resolution diffusion imaging at 3 T. Eur J Radiol 2008;65(1):36–46.

[9] Holdsworth SJ, et al. Robust GRAPPA-accelerated diffusion-weighted readout-segmented (RS)-EPI. Magn Reson Med 2009;62(6):1629–40.

[10] Chen NK, et al. A robust multi-shot scan strategy for high-resolution diffusion weighted MRI enabled by multiplexed sensitivity-encoding (MUSE). Neuroimage 2013;72:41–7.

[11] Zhang Z, et al. Self-feeding MUSE: a robust method for high resolution diffusion imaging using interleaved EPI. Neuroimage 2015;105:552–60.

[12] Forbes KP, et al. PROPELLER MRI: clinical testing of a novel technique for quantification and compensation of head motion. 2001;14(3):215–22.

[13] . Bammer, R., G. Glover, and M. Moseley. Diffusion tensor spiral imaging. in 10th Annual Meeting of the International Society of Magnetic Resonance in Medicine, Honolulu, HI. 2002.

[14] Karampinos DC, et al. High resolution reduced-FOV diffusion tensor imaging of the human pons with multi-shot variable density spiral at 3T. 2008 30th Annual International Conference of the IEEE Engineering in Medicine and Biology Society. IEEE; 2008.

[15] Li TQ, Kim DH, Moseley ME. High-resolution diffusion-weighted imaging with interleaved variable-density spiral acquisitions. J Magn Reson Imaging 2005;21(4):468–75.

[16] Guo H, et al. POCS-enhanced inherent correction of motion-induced phase errors (POCS-ICE) for high-resolution multishot diffusion MRI. Magn Reson Med 2016;75(1):169–80.

[17] Hu Z, et al. Phase-updated regularized SENSE for navigator-free multishot diffusion imaging. Magn Reson Med 2017;78(1):172–81.

[18] Lustig M, Donoho D, Pauly JM. Sparse MRI: the application of compressed sensing

for rapid MR imaging. Magn Reson Med 2007;58(6):1182–95.
[19] Lustig M, et al. Compressed sensing MRI. IEEE Sig Process Mag 2008;25(2):72–82.
[20] Qaisar S, et al. Compressive sensing: from theory to applications, a survey. vol. 15(5). 2013. p. 443–56.
[21] Wu Y, et al. Accelerated MR diffusion tensor imaging using distributed compressed sensing. Magn Reson Med 2014;71(2):763–72.
[22] Huang J, Chen C, Axel LJMri. Fast multi-contrast MRI reconstruction. vol. 32(10). 2014. p. 1344–52.
[23] Sarvotham S, et al. Distributed compressed sensing of jointly sparse signals. Asilomar conference on signals, systems, and computers. 2005.
[24] Shi X, et al. Parallel imaging and compressed sensing combined framework for accelerating high-resolution diffusion tensor imaging using inter-image correlation. Magn Reson Med 2015;73(5):1775–85.
[29] Dai W, et al. Reduced resolution transit delay prescan for quantitative continuous arterial spin labeling perfusion imaging. Magn Reson Med 2012;67(5):1252–65.
[30] F. Huang, et al., Multi-channel image ratio constrained reconstruction and its application for highly accelerated temperature mapping., in ISMRM. 2012: Melbourne, Australia. [Abstract nr 2917].
[31] Huang F. Image ratio constrained reconstruction. ISMRM recon workshop. 2007. [Sedona. Abstract nr 51].
[32] Mistretta CA, et al. Highly constrained backprojection for time-resolved MRI. Magn Reson Med 2006;55(1):30–40.
[33] M, L., et al., L1 SPIR-iT: autocalibrating parallel imaging compressed sensing., in ISMRM. 2009: Kyoto, Japan. [Abstract nr 379].
[34] Lustig M, Pauly JM. SPIRiT: iterative self-consistent parallel imaging reconstruction from arbitrary k-space. Magn Reson Med 2010;64(2):457–71.
[35] Fessler JA, Sutton BP. Nonuniform fast fourier transforms using min-max interpolation. IEEE Trans Sig Process 2003;51(2):560–74.
[36] Fletcher, R. and C.M.J.T.c.j. Reeves, Function minimization by conjugate gradients. 1964. 7(2): p. 149–154.
[37] Hestenes MR, Stiefel E. Methods of conjugate gradients for solving linear systems. vol. 49. Washington, DC: NBS; 1952.
[38] Shewchuk JR. An introduction to the conjugate gradient method without the agonizing pain. Carnegie-Mellon University. Department of Computer Science; 1994.
[39] Liu C, et al. Self-navigated interleaved spiral (SNAILS): application to high-resolution diffusion tensor imaging. Magn Reson Med 2004;52(6):1388–96.
[40] Noll DC, et al. Deblurring for non-2D Fourier transform magnetic resonance imaging. 1992;25(2):319–33.
[41] Man LC, Pauly JM, Macovski AJMrim. Improved automatic off-resonance correction without a field map in spiral imaging. 1997;37(6):906–13.
[42] Jenkinson, M., et al., Fsl. 2012. 62(2): p. 782–790.
[43] Dietrich O, et al. Measurement of signal-to-noise ratios in MR images: influence of multichannel coils, parallel imaging, and reconstruction filters. J Magn Reson Imaging 2007;26(2):375–85.
[44] Reeder SB, et al. Practical approaches to the evaluation of signal-to-noise ratio performance with parallel imaging: application with cardiac imaging and a 32-channel cardiac coil. Magn Reson Med 2005;54(3):748–54.
[45] Setsompop K, et al. Improving diffusion MRI using simultaneous multi-slice echo planar imaging. Neuroimage 2012;63(1):569–80.
[46] X. Ma, F. Huang, and H. Guo, Investigation of number of direction selection for joint reconstruction in multiple-direction diffusion imaging., in ISMRM. 2014: Milan, Italy. Abstract nr 2594.
[47] Dong Z, et al. Motion-corrected k-space reconstruction for interleaved EPI diffusion imaging. Magn Reson Med 2018;79(4):1992–2002.
[48] Wang S, et al. Learning joint-sparse codes for calibration-free parallel MR Imaging. IEEE Trans Med Imaging 2018;37(1):251–61.
[49] Wang S, et al. Iterative feature refinement for accurate undersampled MR image reconstruction. Phys Med Biol 2016;61(9):3291–316.
[50] Gao H, et al. PCLR: phase-constrained low-rank model for compressive diffusion-weighted MRI. Magn Reson Med 2014;72(5):1330–41.